Self-assembled nanostructures in ionic liquids facilitate charge storage at electrified interfaces

Xianwen Mao[*1], Paul Brown[1], Ctirad Červinka[2,3], Gavin Hazell[4], Hua Li[5], Yinying Ren[1], Di Chen[6], Rob Atkin[5], Julian Eastoe[4], Isabelle Grillo[7], Agilio. A. H. Padua[1,2], Margarida. F. Costa Gomes[*1,2], T. Alan Hatton[*1]

[1]*Department of Chemical Engineering, Massachusetts Institute of Technology, 77 Massachusetts Avenue, Cambridge, MA, 02139, United States*

[2]*Ecole Normale Supérieure de Lyon, Laboratoire de Chimie, UMR CNRS 5182, 46 allée d'Italie, 69364 Lyon Cedex 07, France*

[3]*Department of Physical Chemistry, University of Chemistry and Technology, Prague, Technická 5, CZ-166 28 Prague 6, Czech Republic*

[4]*School of Chemistry, University of Bristol, Cantock's Close, Bristol BS8 1TS, United Kingdom*

[5]*School of Molecular Sciences, The University of Western Australia, Perth, WA 6009, Australia*

[6]*Department of Materials Science and Engineering, Stanford University, Stanford, CA 94305*

[7]*Institut Max-von-Laue-Paul-Langevin, BP 156-X, F-38042 Grenoble Cedex, France*

[*]Corresponding author: tahatton@mit.edu (T.A.H.), margarida.costa-gomes@ens-lyon.fr (M.F.C.G.), xmao@mit.edu (X.M.)

ABSTRACT

Driven by the potential applications of ionic liquids (ILs) in many emerging electrochemical technologies, recent research efforts have been directed at understanding the complex ion ordering in these systems, to uncover novel energy storage mechanisms at IL/electrode interfaces. Here, we discover that surface-active ionic liquids (SAILs), which contain amphiphilic structures inducing self-assembly, exhibit enhanced charge storage performance at electrified surfaces. Unlike conventional non-amphiphilic ILs (NAILs), for which ion distribution is dominated by Coulombic interactions, SAILs exhibit significant and competing van der Waals interactions owing to the nonpolar surfactant tails, leading to unusual interfacial ion distributions. We reveal that at an intermediate degree of electrode polarization SAILs display optimal performance, because the low-charge-density alkyl tails are effectively excluded from the electrode surfaces, whereas the formation of nonpolar domains along the

surface suppresses undesired overscreening effects. This work represents a crucial step towards understanding the unique interfacial behavior and electrochemical properties of amphiphilic liquid systems showing long-range ordering, and offers insights into the design principles for high-energy-density electrolytes based on spontaneous self-assembly behavior.

Research interest in ionic liquids (ILs) as electrolytes for energy devices stems from several unique properties such as low volatility and flammability, as well as high electrochemical stability[1-5]. An understanding of the molecular-level interactions between ILs and electrified interfaces is crucial for optimization of device performance[6]. For instance, interfacial IL layers at charged surfaces govern the electric double layer (EDL) structure, a key factor determining the device energy density[2,4,6,7]. The EDL structure with ILs is drastically different from that in aqueous and organic electrolytes[8-10]; the complex ion ordering in ILs exhibits many subtleties, and remains an active area of debate[11-14]. Here we present the first detailed investigation into electrocapacitive characteristics and fundamental EDL structures of an emerging IL class based on surface-active agents, or surface-active ILs (SAILs)[13,15-19]. Our study reveals a novel material design principle for enhancing charge storage owing to the self-assembled nanostructures in amphiphilic liquids, and introduces a class of liquids with long-range ordering, having broad implications for diverse fields, ranging from interfacial science[20,21] to energy technologies[22,23].

SAILs are inherently amphiphilic, and can self-assemble into nanostructures composed of distinct polar and nonpolar domains[13,15-19]. Most previous studies on the IL EDL structure and IL-based energy devices focus on non-amphiphilic ILs (NAILs) where neither ion is based on a classical surfactant structure[6,24]. Whereas nanostructuring was observed under confinement for some NAILs where one of the ions, usually the cation, bears moderate to long chains[25], these nanostructures are weaker – less well defined – than those for SAILs. The bulk phase self-assembled nanostructures of SAILs have been studied previously[17], but how these nanostructures behave at electrified interfaces and are related to EDL structures, critical for energy storage applications, remains unexplored. Compared to NAILs, SAILs have different properties, which challenge the traditional understanding of IL electrochemistry, as speculated previously[26]. Here we show that at elevated temperatures SAILs impart much higher capacitances than NAILs. Molecular dynamics (MD) simulations reveal that the ion distribution, cation-anion correlations, and decay lengths of molecular layering of SAILs are fundamentally different from those of NAILs. The unusual EDL structure of SAILs stems from their

unique ability to self-assemble into highly ordered interfacial nanostructures, which is key for producing high capacitances at intermediate electrode polarizations. The energy densities achievable with neat SAILs at elevated temperatures, or of SAIL-NAIL mixtures at room temperature, exceed those of many known electrolytes (Supplementary Note 6), demonstrating adaptability of SAILs for high-energy-density devices. This proof-of-concept work represents a new paradigm for electrochemical energy storage, through exploitation of the unfavorable interactions between hydrocarbon groups and ionic moieties in amphiphilic electrolytes, to drive partitioning of counterions near the interface, and hence, reduce the EDL thicknesses.

Bulk-phase structural and electrochemical characterization

The SAIL examined here is 1-butyl-3-methylimidazolium 1,4-bis(2-ethylhexoxy)-1,4-dioxobutane-2-sulfonate ($[C_4C_1Im][AOT]$) (Fig. 1a). $[AOT]^-$ is distinctly amphiphilic with a negative charge located at one end of the ion (polar head) and a bulky branched di-chain hydrocarbon group at the other end (nonpolar tail). The control IL is a common NAIL, $[C_4C_1Im][BF_4]$, that contains an identical cation to $[C_4C_1Im][AOT]$ but a smaller, inorganic anion. Temperature-controlled small-angle neutron scattering (SANS) measurements (Fig. 1b) show clearly that $[C_4C_1Im][AOT]$ displays a Bragg peak at $q = 0.28$ Å^{-1}, indicating ordered nanostructures with a repeating unit length scale (d) of ~ 22 Å, consistent with the expected repeat structure for $[C_4C_1Im][AOT]$ (Fig. 1b inset). The SANS is consistent with $[AOT]^-$ bilayers formed via aggregation of the nonpolar tails, with charge neutralizing layers of $[C_4C_1Im]^+$ adjacent to the anionic polar heads. The self-assembly of the $[AOT]^-$ nonpolar tails results in formation of nanoscale nonpolar domains, whereas $[C_4C_1Im]^+$ and the $[AOT]^-$ polar heads form polar domains. In contrast, SANS from $[C_4C_1Im][BF_4]$ does not exhibit a Bragg peak, indicating the absence of any significant long-range ordered nanostructures. Fig. 1c compares the cyclic voltammograms (CVs) of $[C_4C_1Im][BF_4]$ and $[C_4C_1Im][AOT]$, obtained using supercapacitors composed of carbon nanotubes (CNTs) with a Brunauer-Emmett-Teller (BET) surface area of 198 m^2/g (Supplementary Fig. 4 a-c). At 25 °C, the CV for $[C_4C_1Im][AOT]$ shows a more tilted shape and a smaller integral area than that for $[C_4C_1Im][BF_4]$. The CV results suggest a higher ionic resistance and a smaller double-layer capacitance for $[C_4C_1Im][AOT]$, which may be due to its higher viscosity at this temperature (Supplementary Fig. 3c). On increasing temperature the CV integral areas for both ILs increase, consistent with reduced viscosity. However, unexpectedly, at 130 and 200 °C, although $[C_4C_1Im][AOT]$ is still more viscous than

90   [C$_4$C$_1$Im][BF$_4$], the CVs for [C$_4$C$_1$Im][AOT] now exhibit significantly larger integral areas than those

91   for [C$_4$C$_1$Im][BF$_4$]. The CV-derived specific capacitances (Fig. 1d) clearly show that at 130 and 200 □,

92   [C$_4$C$_1$Im][AOT] possesses a remarkably better capacitive energy storage capability than does

93   [C$_4$C$_1$Im][BF$_4$]. Control experiments show that the unusually large capacitances observed for

94   [C$_4$C$_1$Im][AOT] do not result from peculiar electrode properties or high-temperature-operation-induced

95   degradation (Supplementary Note 7).

96

MD simulations reveal anomalous EDL structures in SAILs

98   The observed differences in electrocapacitive performance between [C$_4$C$_1$Im][AOT] and

99   [C$_4$C$_1$Im][BF$_4$] may stem from their distinct molecular architectures, leading to different EDL structures.

100   To understand why [C$_4$C$_1$Im][AOT] outperforms [C$_4$C$_1$Im][BF$_4$] at higher temperatures, we interrogated

101   the detailed EDL structures of the two ILs, confined by electrified graphite surfaces at elevated

102   temperature, via atomistic molecular dynamics (MD) simulations (details in Methods and

103   Supplementary Note 4.1). Fig. 2 a and c show the ion number density (ρ_N, normalized to the bulk value)

104   profiles of [C$_4$C$_1$Im][BF$_4$] and [C$_4$C$_1$Im][AOT], respectively, at electrified interfaces with applied

105   potentials (U) of ± 2 V. The NAIL [C$_4$C$_1$Im][BF$_4$] exhibits a lamellar structure of alternating charges,

106   which persists for ~ eight ion layers (4 distinguishable maxima for cation and anion ρ_N profiles),

107   consistent with previous experimental[11] and theoretical[27] observations of charged-surface-induced long-

108   range molecular layering in common NAILs. Interestingly, [C$_4$C$_1$Im][AOT] displays a different

109   molecular layering behavior: the surface induced charge-alternating structure for [C$_4$C$_1$Im][AOT] only

110   persists for ~ two ion layers, with the first peak showing a much larger ρ_N relative to that of

111   [C$_4$C$_1$Im][BF$_4$]. Notably, the simulated static neutron scattering structure factors for [C$_4$C$_1$Im][AOT] and

112   [C$_4$C$_1$Im][BF$_4$] (Supplementary Fig. 11, Supplementary Note 4.1) match their respective SANS profiles

113   (Fig. 1b)

114   The nanoscale self-assembly of the nonpolar groups in [C$_4$C$_1$Im][AOT] may account for the

115   atypical ion packing behavior at electrified interfaces (Fig. 2 c-d), being in stark contrast to the

116   conventional behavior of NAILs (Fig. 2 a-b). At neutral interfaces, the bulk microscopic structure of

117   [C$_4$C$_1$Im][AOT] is characterized by the formation of charged polar domains and nonpolar domains (Fig.

118   1b inset). Introduction of surface charges then induce alignment of charged domains along the interface.

119   Near a positively charged surface, the polar heads of [AOT]$^-$ are electrostatically attracted to the

interface, whereas the nonpolar tails orientate outward, in close proximity to the nonpolar tails of the next $[AOT]^-$ layer, thus forming a bilayer parallel to the positively charged surface, with a neutralizing $[C_4C_1Im]^+$ layer adjacent to the anionic polar heads of $[AOT]^-$. At a negatively charged surface, the innermost ion layer is enriched in $[C_4C_1Im]^+$ cations which fully neutralize the adjacent anionic $[AOT]^-$ bilayer (i.e., the presence of an $[AOT]^-$ bilayer squeezes excess cations into the first ion layer near the interface). The ability to pack *excess* ions at charged interfaces is an advantageous feature of SAILs compared to NAILs, and is driven by the unfavorable interaction between the hydrocarbon and ionic groups compared to cation-anion interactions. Another unexpected finding for $[C_4C_1Im][AOT]$ is that the cation and anion ρ_N profiles beyond the first two ion layers are *positively* correlated (Fig. 2e, right panel), possibly due to the co-movement of $[C_4C_1Im]^+$ cations and $[AOT]^-$ polar heads. The nonpolar tail-tail interaction could lead to the confinement of small $[C_4C_1Im]^+$ cations and $[AOT]^-$ polar heads within the polar domains. With short-alkyl-chain NAILs, which cannot self-assemble, the ion-ion electrostatic interactions alone dictate that the anionic density reaches a maximum where the cationic density reaches a minimum, which should result in negatively-correlated anion-cation spatial distributions (Fig. 2e, left panel).

The ability of $[C_4C_1Im][AOT]$ to pack excess ions at the interface and the positive correlation between the cation and anion spatial distribution suggests that $[C_4C_1Im][AOT]$ should reach bulk electroneutrality over shorter distances than $[C_4C_1Im][BF_4]$, which can be validated by calculating the net charge density (ρ_Q) distributions (Fig. 2f). The NAIL $[C_4C_1Im][BF_4]$ shows a pronounced ρ_Q oscillatory pattern before reaching electroneutrality at around 30 □ from the surface. In contrast, the amplitude of ρ_Q oscillation for $[C_4C_1Im][AOT]$ diminishes more quickly, and decays to its bulk value around 10 □ from the surface. The decay length (ξ) of the charge oscillation, quantified using an envelope function that confines the ρ_Q profile (Supplementary Note 4.2), is shown in Fig. 2g as a function of U. Compared to $[C_4C_1Im][BF_4]$, $[C_4C_1Im][AOT]$ generally exhibits smaller ξ values, indicating thinner EDLs and thus larger capacitances. The calculated differential capacitances (C_d) (Fig. 2h; Supplementary Note 4.2) show that with intermediate electrode polarization (i.e., $1\ V < |U| < 2\ V$) $[C_4C_1Im][AOT]$ generally exhibits higher differential capacitances than does $[C_4C_1Im][BF_4]$. However, at low electrode polarization (i.e, U is near 0 V), $[C_4C_1Im][AOT]$ shows lower capacitances than $[C_4C_1Im][BF_4]$, probably because near the electrode surface the former has a larger density of $[AOT]^-$ nonpolar tails (i.e., latent voids), reducing the near-surface charge density (Supplementary Fig. 12). By contrast, at intermediate polarization (i.e., $|U|$ is about 1 to 2 V), those nonpolar tails do not partition to

151 the electrode surface (Supplementary Fig. 12), resulting in ~22 □ wide nonpolar domains parallel to the

152 electrode surface. This prevents the development of strongly oscillating, cation-anion alternating

153 structure, commonly observed in NAILs, that would lead to overscreening and EDL thickening. The role

154 of such nonpolar domains in preventing overscreening effects may be analogous to that played by a

155 second electrode wall inside a nanopore[28]. The potential-dependent rearrangement of the [AOT]$^-$

156 nonpolar tails, revealed by these atomistic MD simulations, agrees with earlier studies based on Monte

157 Carlo simulations of liquids with elongated ions containing charged "heads" and neutral "tails"[29,30]. At

158 high electrode polarization (i.e., $|U| > 2$ V), lattice saturation effects due to the steric constraints of finite

159 ion sizes[6,7] occur, and the capacitances of both [C$_4$C$_1$Im][AOT] and [C$_4$C$_1$Im][BF$_4$] will decrease.

160 Additionally, the thinner EDL (and thus shorter Debye length) for [C$_4$C$_1$Im][AOT] relative to that of

161 [C$_4$C$_1$Im][BF$_4$] at intermediate electrode polarization implies a higher *free* ion concentration in the

162 former. In the EDL of [C$_4$C$_1$Im][BF$_4$], as in other NAILs[8,10], most cations and anions are strongly

163 associated to form "neutral aggregates" (Fig. 2b) which contribute weakly to the free ion concentration.

164 By contrast, in the EDL of [C$_4$C$_1$Im][AOT], due to its amphiphilic nature, only half the population of the

165 first counterion layer could form neutral aggregates with the neighboring co-ion layer, resulting in

166 abundant free counter-ions at the interface (Fig. 2d). Additional constant-surface-charge simulations

167 (Supplementary Fig. 7) yielded consistent results with those shown here by the constant-surface-

168 potential method (Fig. 2).

169

Elucidation of interfacial nanostructures by atomic force microscopy

171   Atomic force microscopy (AFM) measurements were performed to examine the nanoscale

172 molecular layering of these ionic liquids at a graphite electrode (for experimental details, see Methods

173 and Supplementary Note 5). It is recognized that ionic liquids form layered structures near solid surfaces,

174 which are referred to as interfacial nanostructures[31-35]. The AFM force-distance profiles for

175 [C$_4$C$_1$Im][BF$_4$] and [C$_4$C$_1$Im][AOT] (Fig. 3) consist of a series of pronounced, discrete steps, produced

176 by the AFM tip pushing up against, and then rupturing, interfacial layers. The "rupture force" for an IL

177 layer is reflected by the maximum of each step; a larger rupture force indicates a higher degree of

178 ordering (i.e., stronger cohesive interactions) in the ion layer. For both ILs, at the open circuit potential

179 (OCP), the data reveal only two steps with small rupture forces, indicating weak interfacial structures,

180 whereas with applied biases (OCP $\pm$ 1 V) at least four steps are seen, with much higher rupture forces,

181   indicating stronger ordering of interfacial nanostructures. Additionally, for all the three cases (at OCP,

182   OCP − 1 V and OCP + 1 V), the rupture force decreases more rapidly with layer number for

183    $[C_4C_1Im][AOT]$ than $[C_4C_1Im][BF_4]$, which matches well the simulations described above (Fig. 2 a and

184   c). Moreover, the rupture force for step I is higher for $[C_4C_1Im][AOT]$ than for $[C_4C_1Im][BF_4]$, again

185   consistent with the simulations (Fig. 2 a and c) showing that ρ_N of the innermost layer is much larger for

186    $[C_4C_1Im][AOT]$ than for $[C_4C_1Im][BF_4]$.

187   The separation between two adjacent steps (i.e., between steps I/II, II/III, or III/IV shown in Fig.

188   3) for $[C_4C_1Im][BF_4]$ and $[C_4C_1Im][AOT]$ is notably different. For $[C_4C_1Im][BF_4]$ the separation is 6-7

189   Å (corresponding to the physical dimension of an ion pair of $[C_4C_1Im]^+$ and $[BF_4]^-$), in accordance with

190   the MD simulations (Fig. 2a, schematically illustrated by orange double arrows in Fig. 2b). In stark

191   contrast, the separation between steps for $[C_4C_1Im][AOT]$ is three to four times larger (22-24 Å), in

192   good agreement with both the repeating unit length scale measured by SANS (Fig. 1b) and the

193   simulations (Fig. 2c, schematically illustrated by orange double arrows in Fig. 2d). For $[C_4C_1Im][BF_4]$,

194   with applied biases of ± 1 V, the separation between the electrode surface and step I (corresponding to

195   the layer nearest to the surface) is about 2-3 Å, indicating a single ion layer (either cation or anion,

196   depending on the applied bias, as shown by the green double arrow in Fig. 2b). This agrees well with the

197   simulated ion number density profiles, indicating the first ion layer is about 2-3 Å thick (Fig. 2a). For

198    $[C_4C_1Im][AOT]$, at OCP − 1 V, the separation between the electrode surface and step I is about 4 Å,

199   corresponding to a cation-rich layer, also consistent with the simulations (Fig. 2c, left; green double

200   arrow in Fig. 2d, left). For $[C_4C_1Im][AOT]$ at OCP + 1V, step I is about 6 Å thick, consistent with

201   simulations (Fig 2c, right; green double arrow in Fig. 2d, right), but much smaller than the distance

202   expected for an $[AOT]^-$ double layer. This is a consequence of the $[AOT]^-$ neutral tails tending to

203   orientate towards the electrode surface through solvophobic interactions (Supplementary Fig. 12). These

204   force measurements unambiguously confirm the fundamentally different interfacial nanostructures

205   between $[C_4C_1Im][AOT]$ and $[C_4C_1Im][BF_4]$ as suggested by the MD simulations. While high-energy x-

206   ray reflectivity (XRR) measurements may be used to elucidate interfacial nanostructures of ionic

207   liquids[11], we could not obtain good XRR signals for our IL systems, possibly due to the difficulty of

208   preparing a thin, uniform IL film with high stability under x-ray exposure (Supplementary Note 5).

209

210   **EDL properties probed by impedance measurements**

211   To further examine how the EDL capacitances of $[C_4C_1Im][AOT]$ and $[C_4C_1Im][BF_4]$ vary with

212   applied potential, impedance measurements (Methods and Supplementary Note 3) were performed to

213   obtain the differential capacitance *versus* potential profile for both ILs (Fig. 4), using a glassy carbon

214   electrode consisting of a flat IL/graphite interface. With increasing temperature, the capacitances of both

215   ILs become larger consistent with decreasing viscosities, in accordance with the CV measurements in a

216   supercapacitor device (Fig. 1d). More importantly, the capacitance curve of $[C_4C_1Im][AOT]$ is

217   characterized by a minimum at small $|U|$ and two maxima at intermediate $|U|$, whereas that for

218      $[C_4C_1Im][BF_4]$ exhibits a bell-like shape. These capacitance profiles for $[C_4C_1Im][AOT]$ and

219      $[C_4C_1Im][BF_4]$ agree generally with the simulations (Fig. 2h), re-emphasizing fundamental differences

220   in the EDL structures between SAILs and NAILs. Certain fine features, such as the exact positions of

221   minima and maxima in the capacitance curves differ between the simulations and experimental data,

222   possibly due to factors such as specific adsorption or local dielectric properties which are not accurately

223   captured by the simulations. Notably, the experimentally measured capacitances here are not dictated by

224   the quantum capacitances of the carbon electrodes employed, and reflect faithfully the EDL capacitances

225   of the ionic liquids investigated (Supplementary Note 8).

226

Generality, applicability and limitations of SAILs

228   We simulated the EDL structures of two other SAILs sharing the same $[C_4C_1Im]^+$ cation as

229      $[C_4C_1Im][AOT]$, but with different anions: dodecylsulfonate ($[DDS]^-$ single-chain surfactant anion) and

230   1,5-bis(hexyloxy)-3-((hexyloxy)carbonyl)-1,5-dioxopentane-2-sulfonate ($[TC]^-$ tri-chain surfactant

231   anion) (Fig. 5a). These other SAILs show significant structural variations compared to $[AOT]^-$. The

232   simulations indicate that, compared to $[C_4C_1Im][BF_4]$, both $[C_4C_1Im][DDS]$ and $[C_4C_1Im][TC]$ also

233   exhibit diminished ρ_Q oscillations (Fig. 5b) and a thinner EDLs (Fig. 5c) at intermediate electrode

234   polarizations (i.e., surface charge density $\sigma = \pm 5$ and ± 10 $\mu C/cm^2$), suggesting that these may be

235   generic features of SAILs. To validate that MD captures the self-assembly behavior shown by SANS,

236   additional simulations were performed using uncharged confining surfaces at a lower temperature of

237   100 □. Such conditions allow for the study of SAIL structures in the absence of an electric field, and

238   with suppressed thermal fluctuations, so that the nonpolar domains align parallel to the confining surface

239   (Fig. 5d, left) instead of assuming random orientations (Fig. 5d, right). Therefore, the repeating

240   structures of SAILs along the *z*-axis normal to the interface can be visualized directly. Fig. 5e shows

241 clearly that the three SAILs, [C$_4$C$_1$Im][DDS], [C$_4$C$_1$Im][AOT] and [C$_4$C$_1$Im][TC], display a periodic ρ_N

242 pattern reflecting their repeating nanostructures, lacked by the profile for [C$_4$C$_1$Im][BF$_4$]. The average

243 peak spacing in the ρ_N patterns appears to decrease from [C$_4$C$_1$Im][DDS] to [C$_4$C$_1$Im][AOT] to

244 [C$_4$C$_1$Im][TC], consistent with the reduction in anion size/length ([DDS]$^-$ > [AOT]$^-$ > [TC]$^-$) as well as

245 the decreasing characteristic length of repeating structures measured by small-angle X-ray scattering

246 ([C$_4$C$_1$Im][DDS] = 22.9 □, [C$_4$C$_1$Im][AOT] = 21.5 □, [C$_4$C$_1$Im][TC] = 18.8 □)[19].

247   To validate experimentally that SAILs generally outperform NAILs at elevated temperatures, we

248 synthesized three other SAILs, [C$_4$C$_1$Im][C$_8$SO$_4$], [C$_4$C$_1$Im][C$_{10}$SO$_4$] and [C$_4$C$_1$Im][C$_{12}$SO$_4$]

249 (Supplementary Fig. 10 and Supplementary Table 6). Their SANS profiles (Fig. 6a) at 70 □ display

250 clear Bragg peaks at q = 0.24, 0.22 and 0.22 □$^{-1}$, respectively, indicating repeat structures with

251 characteristic dimensions of 26, 28 and 28 □, respectively. The SANS profiles at 25 and 50 □ for

252 [C$_4$C$_1$Im][C$_8$SO$_4$] and [C$_4$C$_1$Im][C$_{10}$SO$_4$] are similar to those at 70 □. The long chain analogue

253 [C$_4$C$_1$Im][C$_{12}$SO$_4$] is solid at low temperatures (25 and 50 □), resulting a Bragg peak at q = 0.31 □$^{-1}$.

254 Fig. 6b depicts the specific capacitances (left axis) of the three SAILs (using CNT supercapacitors),

255 together with the enhancement (right axis) relative to those of [C$_4$C$_1$Im][BF$_4$]. Relative to

256 [C$_4$C$_1$Im][BF$_4$], and at high temperature (130 □), these SAILs exhibit larger capacitances with a two- to

257 three-fold enhancement, similar to the findings with [C$_4$C$_1$Im][AOT] (Supplementary Fig. 6).

258   The energy storage performance of SAILs depends not only on temperature but also on the

259 operating voltage window. For example, whether [C$_4$C$_1$Im][AOT] exhibits larger or smaller differential

260 capacitances than [C$_4$C$_1$Im][BF$_4$] depends on the degree of electrode polarization (i.e. the applied

261 potential), as shown experimentally (Fig. 4) and also via MD simulations (Fig. 2h). Therefore, when

262 operating over a wide voltage window, a supercapacitor with [C$_4$C$_1$Im][AOT] should show larger

263 capacitances than if [C$_4$C$_1$Im][BF$_4$]is used, whereas when operating over a narrow voltage window, the

264 order is reversed. However, [C$_4$C$_1$Im][AOT] is preferred for energy storage applications because in

265 practice it is advantageous to have large capacitances when operating over broad voltage windows since

266 energy density scales as $\int_0^V CU dU$ or CV^2, where C is the capacitance, U is the applied potential, and V

267 is the operating voltage window.

268   The Ragone plot (Supplementary Fig. 14) shows that at low temperatures, the high viscosity of

269 [C$_4$C$_1$Im][AOT] results in energy density/power density combinations that are worse than those of

270 [C$_4$C$_1$Im][BF$_4$]. However, at high temperatures where [C$_4$C$_1$Im][AOT] is more fluid, it outperforms

271     $[C_4C_1Im][BF_4]$ in terms of both energy and power density, making $[C_4C_1Im][AOT]$ particularly suitable

272   for important high-temperature applications[36]. Also, mixing $[C_4C_1Im][AOT]$ with $[C_4C_1Im][BF_4]$ led to

273   higher capacitances than those of individual component alone at room temperature (Supplementary Fig.

274   9), suggesting a path to engineer SAIL-based energy devices for low-temperature uses. Due to their

275   larger ion sizes, SAILs might not adsorb so easily into ultranarrow pores with certain porous carbon

276   electrodes[37]; however, SAILs could be used in combination with other nonporous high-surface-area

277   electrodes such as onion-like carbon[38], carbon nanocage[39] and carbon fibers[40,41]. Moreover, the

278   electrocapacitive performance of SAILs depends on the specific chemical structure (e.g., the length of

279   the alkyl chains), because these determine the strength of interactions between alkyl chains, as well as

280   between the electrode surfaces and alkyl chains. Therefore, SAIL chemical architecture dictates i) how

281   the density of neutral tails varies with the applied potential, and ii) how effective the self-assembled

282   nonpolar domains are for preventing overscreening. These two factors combined would ultimately

283   determine the shape of the capacitance *versus* potential profile, which can provide direct information on

284   the performance of SAILs and the desired operation voltages.

285

286   In conclusion, this study reveals a fundamentally new interfacial phenomenon where the self-

287   assembled nanostructures in ionic liquids facilitate charge storage at electrified surfaces. This paves the

288   way for building "designer" SAILs, since there are a huge number of possible anion-cation

289   combinations that can be employed to fine-tune the self-assembled nanostructures of SAILs and hence

290   control interfacial electrochemical properties. Additionally, due to exceptional stability and tunable

291   electrochemical performance, rationally engineered SAILs could be used for a wide array of next-

292   generation electrochemical devices for improved safety (e.g., avoidance of flammable organic

293   electrolytes in batteries[42]), and afford electrochemical modulation *in vivo* (e.g., drug delivery[43]) or for

294   gas-based applications (e.g., CO_2 capture[44], gas sensing[45], biomimetic multiphase transport[46]). More

295   broadly, the self-assembly-based charge storage mechanism discovered here offers a new approach for

296   optimizing interfacial electrochemical behavior of other fluids with ordered nanostructures beyond

297   SAILs (e.g., liquid crystals, block copolymer electrolytes, emulsions), and could have profound impacts

298   on related emerging technologies.

299
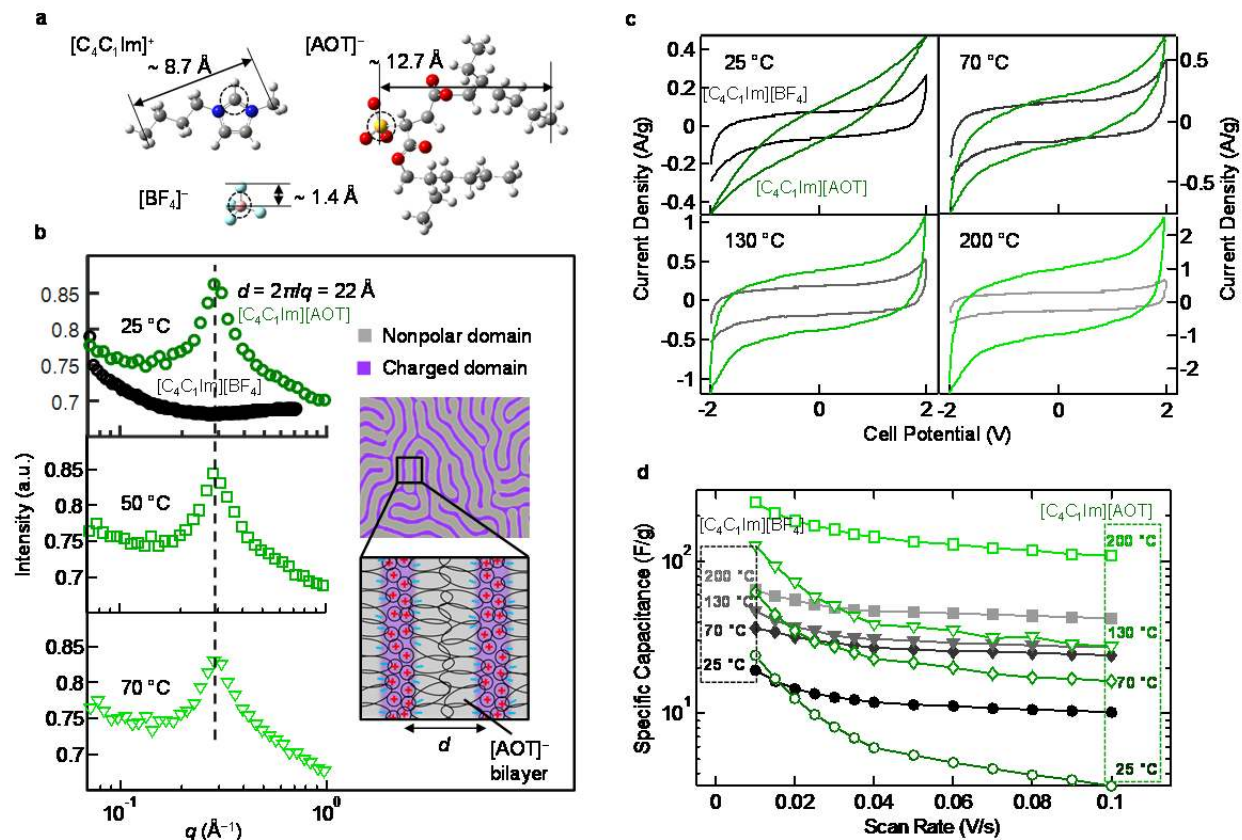
Fig. 1. **Bulk-phase structural and electrochemical characterization of [C₄C₁Im][AOT]. a**, Molecular structures of $[C_4C_1Im]^+$, $[BF_4]^-$, and $[AOT]^-$ (H = white, C = gray, N = blue, S = yellow, O = red, B = pink, F = cyan). Typical distances in the molecular ions are indicated. **b**, SANS profiles of $[C_4C_1Im][BF_4]$ (25 □) and $[C_4C_1Im][AOT]$ (25, 50, 70 □). Inset: illustration of self-assembly of $[C_4C_1Im][AOT]$ leading to a repeating nanostructure comprising $[AOT]^-$ bilayers (red: cation; blue: anion). Simulated SANS profiles (Supplementary Fig. 11) are consistent with the experimental data. **c-d**, CV profiles (scan rate = 20 mV/s) (**c**) and specific capacitance *versus* scan rate (**d**) for $[C_4C_1Im][BF_4]$ or $[C_4C_1Im][AOT]$ at 25, 70, 130 and 200 □.
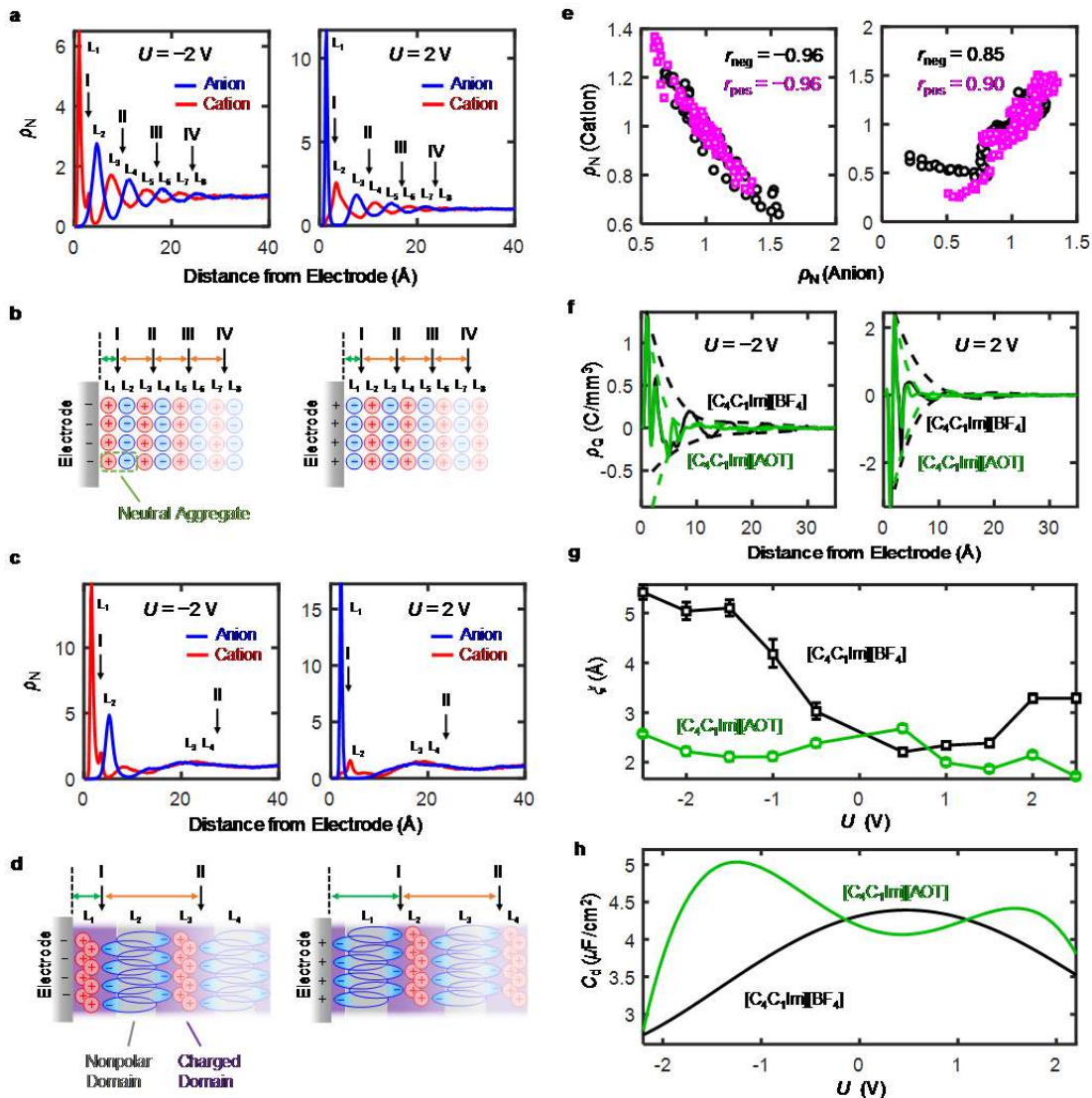
Fig. 2. MD simulations reveal unusual EDL structures of [C$_4$C$_1$Im][AOT]. a-d, Ion number density (ρ_N) profile obtained from MD simulations and schematic illustration of hypothesized ion arrangement for [C$_4$C$_1$Im][BF$_4$] (**a**, **b**) and [C$_4$C$_1$Im][AOT] (**c**, **d**) at negatively (left panel) and positively (right panel) charged interfaces with applied potentials (U) of ± 2 V. Black arrows with I, II, III and IV indicate possible positions corresponding to the AFM push-through locations (Fig. 3). **e**, Correlations between the cationic and anionic ρ_N obtained at positively (magenta, $U = 2$ V) and negatively (black, $U = -2$ V) charged interfaces for [C$_4$C$_1$Im][BF$_4$] (left panel) and [C$_4$C$_1$Im][AOT] (right panel) for the distance range of 10 to 40 □ away from the interface. r_{neg} and r_{pos} are the Pearson correlation coefficients for negatively and positively charged interfaces, respectively. **f**, Net charge density (ρ_Q) profiles (solid line) and corresponding envelope functions (dashed line) of [C$_4$C$_1$Im][BF$_4$] and [C$_4$C$_1$Im][AOT] at negatively (left panel, $U = -2$ V) and positively (right panel, $U = 2$ V) charged interfaces. **g-h**, Decay length (ξ) of the surface-induced ion layering (**g**) and differential capacitance (C_d) (**f**) as a function of U for [C$_4$C$_1$Im][BF$_4$] and [C$_4$C$_1$Im][AOT].
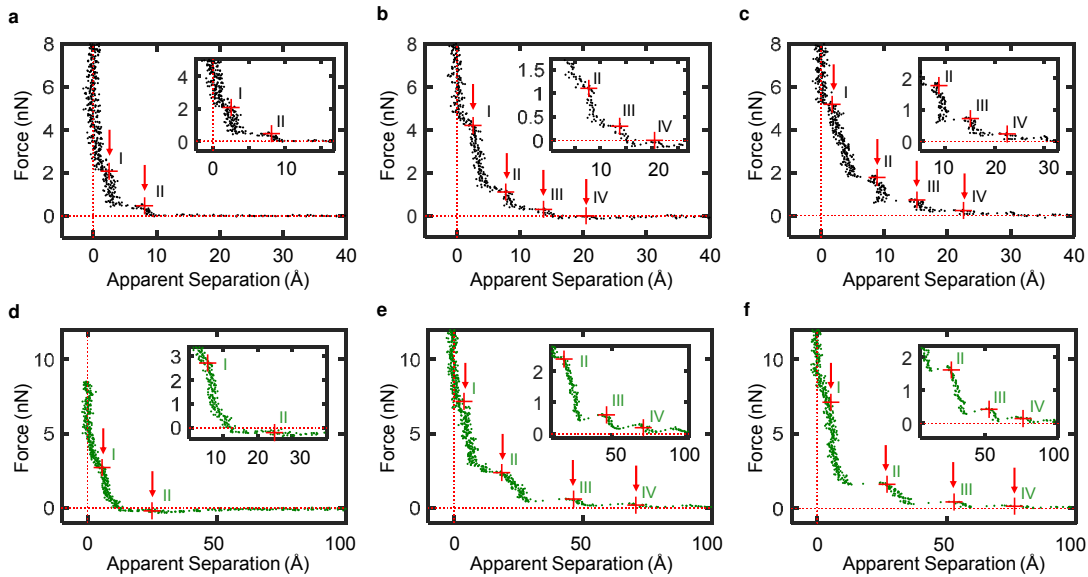
Fig. 3. Elucidation of interfacial molecular layering through AFM force measurements. a-c, Force *versus* apparent separation profiles obtained with a silica colloid probe approaching a graphite electrode surface immersed in $[C_4C_1Im][BF_4]$ at OCP (**a**), OCP − 1 V (**b**), and OCP + 1 V (**c**). Inset: zoom-in of the lower force regime. Red cross with I, II, III or IV indicates the location of each discrete step and the "rupture force" magnitude. **d-f**, same as **a-c** but for the case of $[C_4C_1Im][AOT]$.
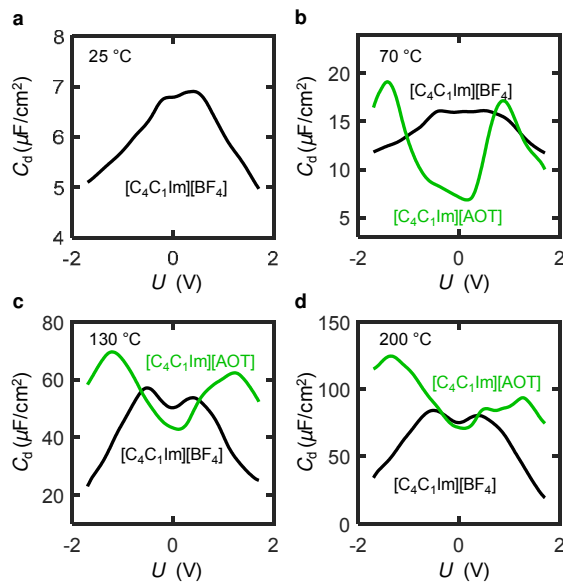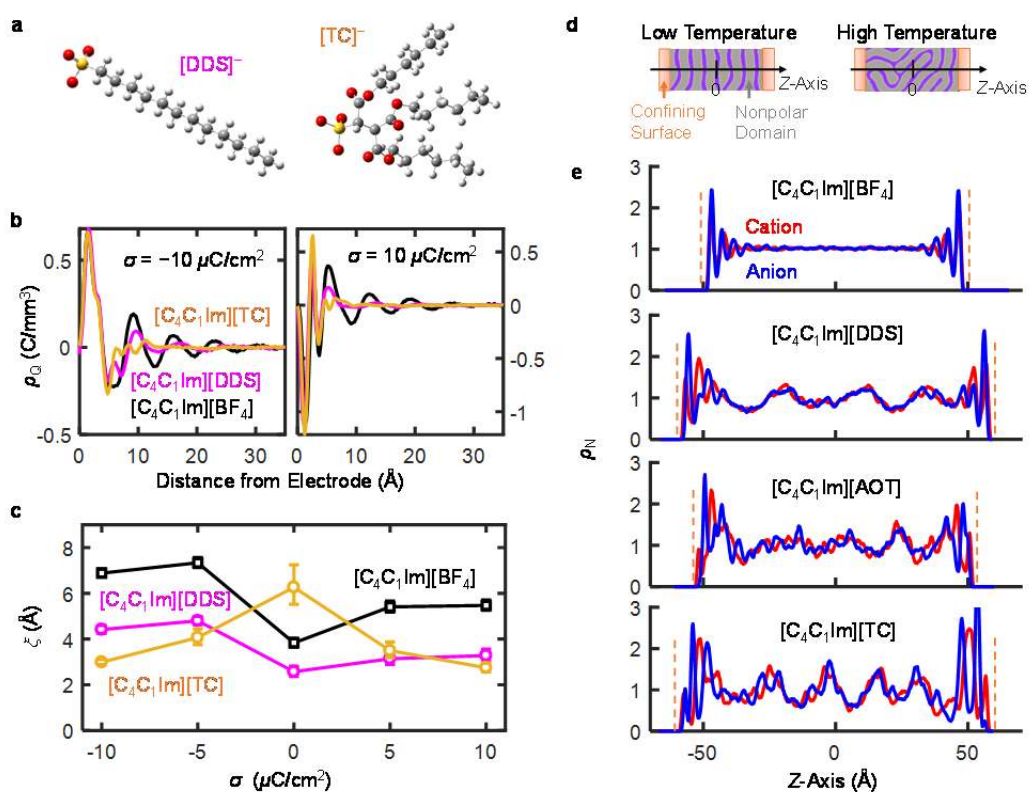

Fig. 4. EDL properties probed by impedance measurements. Experimentally determined differential capacitances as a function of the applied potential (U, versus OCP) for $[C_4C_1Im][BF_4]$ and $[C_4C_1Im][AOT]$ at 25 □ (**a**), 70 □ (**b**), 130 □ (**c**), and 200 □ (**d**) on a glassy carbon electrode.

Fig. 5. MD simulations of other SAILs. a, Molecular structures of [DDS]$^-$ and [TC]$^-$ (H = white, C = gray, S = yellow, O = red). **b**, Net charge density (ρ_Q) profiles of [C$_4$C$_1$Im][DDS], [C$_4$C$_1$Im][TC] and [C$_4$C$_1$Im][BF$_4$] at negatively (left panel) and positively (right panel) charged interfaces. **c**, Decay length (ξ) versus σ for [C$_4$C$_1$Im][DDS], [C$_4$C$_1$Im][TC] and [C$_4$C$_1$Im][BF$_4$]. **d**, Schematic illustration of the possible orientations of nonpolar domains in SAILs at low (left) and high (right) temperatures. **e**, Ion number density (ρ_N) profiles of [C$_4$C$_1$Im][BF$_4$], [C$_4$C$_1$Im][DDS], [C$_4$C$_1$Im][AOT] and [C$_4$C$_1$Im][TC] at 100 □ with zero charge on the confining surface. Dashed line: position of the IL/solid interface.
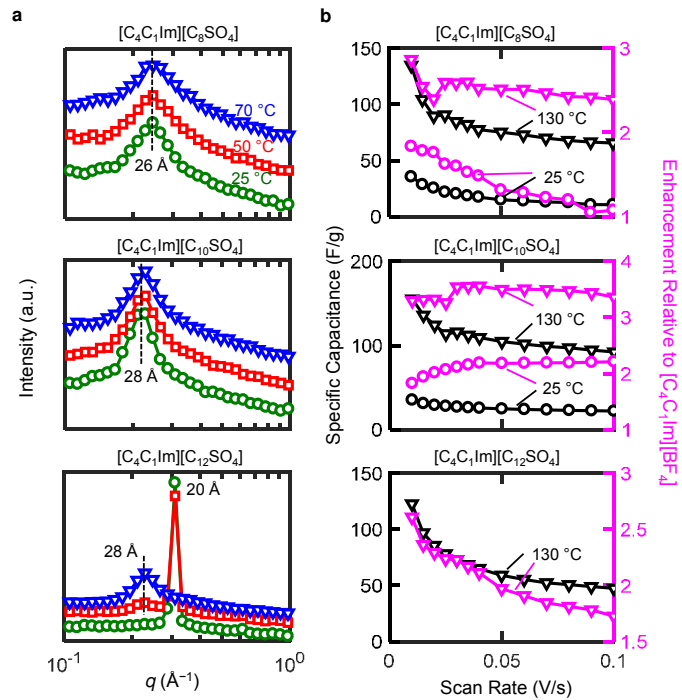
349

Fig. 6. Electrocapacitive performance of other SAILs. a, SANS profiles of $[C_4C_1Im][C_8SO_4]$, $[C_4C_1Im][C_{10}SO_4]$ and $[C_4C_1Im][C_{12}SO_4]$ at 25, 50 and 70 □. **b**, Specific capacitance (left axis) *versus* scan rate for $[C_4C_1Im][C_8SO_4]$ (25 and 130 □), $[C_4C_1Im][C_{10}SO_4]$ (25 and 130 □) or $[C_4C_1Im][C_{12}SO_4]$ (130 □), together with the enhancement factor (right axis) compared to the performance of $[C_4C_1Im][BF_4]$.

354

355

356

References

358 1 MacFarlane, D. R., Forsyth, M., Howlett, P. C., Kar, M., Passerini, S., Pringle, J. M., Ohno, H., Watanabe, M., Yan, F., Zheng, W. J., Zhang, S. G. & Zhang, J. Ionic liquids and their solid-state analogues as materials for energy generation and storage. *Nature Reviews Materials* **1**, (2016).

361 2 Salanne, M., Rotenberg, B., Naoi, K., Kaneko, K., Taberna, P. L., Grey, C. P., Dunn, B. & Simon, P. Efficient storage mechanisms for building better supercapacitors. *Nature Energy* **1**, (2016).

363 3 Li, Y., Wang, X. G., Dong, S. M., Chen, X. & Cui, G. L. Recent Advances in Non-Aqueous Electrolyte for Rechargeable Li-O-2 Batteries. *Advanced Energy Materials* **6**, (2016).

365 4 Armand, M., Endres, F., MacFarlane, D. R., Ohno, H. & Scrosati, B. Ionic-liquid materials for the electrochemical challenges of the future. *Nature Materials* **8**, 621-629, (2009).

367 5 Che, H. Y., Chen, S. L., Xie, Y. Y., Wang, H., Amine, K., Liao, X. Z. & Ma, Z. F. Electrolyte design strategies and research progress for room-temperature sodium-ion batteries. *Energy & Environmental Science* **10**, 1075-1101, (2017).

370 6 Fedorov, M. V. & Kornyshev, A. A. Ionic Liquids at Electrified Interfaces. *Chemical Reviews* **114**, 2978-3036, (2014).

372 7 Bazant, M. Z., Storey, B. D. & Kornyshev, A. A. Double Layer in Ionic Liquids: Overscreening versus Crowding. *Physical Review Letters* **106**, (2011).

374 8 Gebbie, M. A., Dobbs, H. A., Valtiner, M. & Israelachvili, J. N. Long-range electrostatic screening in ionic liquids. *Proceedings of the National Academy of Sciences of the United States of America* **112**, 7432-7437, (2015).

377 9 Zhou, H., Rouha, M., Feng, G., Lee, S. S., Docherty, H., Fenter, P., Cummings, P. T., Fulvio, P. F., Dai, S., McDonough, J., Presser, V. & Gogotsi, Y. Nanoscale Perturbations of Room Temperature Ionic Liquid Structure at Charged and Uncharged Interfaces. *Acs Nano* **6**, 9818-9827, (2012).

380 10 Gebbie, M. A., Valtiner, M., Banquy, X., Fox, E. T., Henderson, W. A. & Israelachvili, J. N. Ionic liquids behave as dilute electrolyte solutions. *Proceedings of the National Academy of Sciences of the United States of America* **110**, 9674-9679, (2013).

383 11 Mezger, M., Schroder, H., Reichert, H., Schramm, S., Okasinski, J. S., Schoder, S., Honkimaki, V., Deutsch, M., Ocko, B. M., Ralston, J., Rohwerder, M., Stratmann, M. & Dosch, H. Molecular layering of fluorinated ionic liquids at a charged sapphire (0001) surface. *Science* **322**, 424-428, (2008).

386 12 Crowhurst, L., Lancaster, N. L., Arlandis, J. M. P. & Welton, T. Manipulating solute nucleophilicity with room temperature ionic liquids. *Journal of the American Chemical Society* **126**, 11549-11555, (2004).

388 13 Zhang, S. G., Zhang, J. H., Zhang, Y. & Deng, Y. Q. Nanoconfined Ionic Liquids. *Chemical Reviews* **117**, 6755-6833, (2017).

390 14 Elbourne, A., Voitchovsky, K., Warr, G. G. & Atkin, R. Ion structure controls ionic liquid near-surface and interfacial nanostructure. *Chemical Science* **6**, 527-536, (2015).

392 15 Lopes, J. N. A. C. & Padua, A. A. H. Nanostructural organization in ionic liquids. *Journal of Physical Chemistry B* **110**, 3330-3335, (2006).

394 16 Padua, A. A. H., Gomes, M. F. & Lopes, J. N. A. C. Molecular solutes in ionic liquids: A structural, perspective. *Accounts of Chemical Research* **40**, 1087-1096, (2007).

396 17 Dong, K., Liu, X. M., Dong, H. F., Zhang, X. P. & Zhang, S. J. Multiscale Studies on Ionic Liquids. *Chemical Reviews* **117**, 6636-6695, (2017).

398 18 McDonald, S., Murphy, T., Imberti, S., Warr, G. G. & Atkin, R. Amphiphilically Nanostructured Deep Eutectic Solvents. *The Journal of Physical Chemistry Letters* **9**, 3922-3927, (2018).

400 19 Brown, P., Butts, C. P., Eastoe, J., Fermin, D., Grillo, I., Lee, H.-C., Parker, D., Plana, D. & Richardson, R. M. Anionic Surfactant Ionic Liquids with 1-Butyl-3-methyl-imidazolium Cations: Characterization and Application. *Langmuir* **28**, 2502-2509, (2012).

403 20 Kim, Y. K., Wang, X. G., Mondkar, P., Bukusoglu, E. & Abbott, N. L. Self-reporting and self-regulating liquid crystals. *Nature* **557**, 539-+, (2018).

405 21 Futamura, R., Iiyama, T., Takasaki, Y., Gogotsi, Y., Biggs, M. J., Salanne, M., Segalini, J., Simon, P. &
406   Kaneko, K. Partial breaking of the Coulombic ordering of ionic liquids confined in carbon nanopores.
407   *Nature Materials* **16**, 1225-+, (2017).
408 22 Mefford, J. T., Hardin, W. G., Dai, S., Johnston, K. P. & Stevenson, K. J. Anion charge storage through
409   oxygen intercalation in LaMnO3 perovskite pseudocapacitor electrodes. *Nature Materials* **13**, 726-732,
410   (2014).
411 23 Xia, Y., Mathis, T. S., Zhao, M. Q., Anasori, B., Dang, A., Zhou, Z. H., Cho, H., Gogotsi, Y. & Yang, S.
412   Thickness - independent capacitance of vertically aligned liquid-crystalline MXenes. *Nature* **557**, 409-+,
413   (2018).
414 24 Zhong, C., Deng, Y. D., Hu, W. B., Qiao, J. L., Zhang, L. & Zhang, J. J. A review of electrolyte materials
415   and compositions for electrochemical supercapacitors. *Chemical Society Reviews* **44**, 7484-7539, (2015).
416 25 Smith, A. M., Lovelock, K. R. J., Gosvami, N. N., Licence, P., Dolan, A., Welton, T. & Perkin, S.
417   Monolayer to Bilayer Structural Transition in Confined Pyrrolidinium-Based Ionic Liquids. *The Journal
418   of Physical Chemistry Letters* **4**, 378-382, (2013).
419 26 Kornyshev, A. A. Double-Layer in Ionic Liquids: Paradigm Change? *The Journal of Physical Chemistry
420   B* **111**, 5545-5557, (2007).
421 27 Pak, A. J., Paekw, E. & Hwang, G. S. Relative contributions of quantum and double layer capacitance to
422   the supercapacitor performance of carbon nanotubes in an ionic liquid. *Physical Chemistry Chemical
423   Physics* **15**, 19741-19747, (2013).
424 28 Merlet, C., Rotenberg, B., Madden, P. A., Taberna, P.-L., Simon, P., Gogotsi, Y. & Salanne, M. On the
425   molecular origin of supercapacitance in nanoporous carbon electrodes. *Nature Materials* **11**, 306, (2012).
426 29 Fedorov, M. V., Georgi, N. & Kornyshev, A. A. Double layer in ionic liquids: The nature of the camel
427   shape of capacitance. *Electrochemistry Communications* **12**, 296-299, (2010).
428 30 Georgi, N., Kornyshev, A. A. & Fedorov, M. V. The anatomy of the double layer and capacitance in ionic
429   liquids with anisotropic ions: Electrostriction vs. lattice saturation. *Journal of Electroanalytical Chemistry*
430   **649**, 261-267, (2010).
431 31 Perkin, S., Crowhurst, L., Niedermeyer, H., Welton, T., Smith, A. M. & Gosvami, N. N. Self-assembly in
432   the electrical double layer of ionic liquids. *Chemical Communications* **47**, 6572-6574, (2011).
433 32 Hayes, R., Warr, G. G. & Atkin, R. Structure and Nanostructure in Ionic Liquids. *Chemical Reviews* **115**,
434   6357-6426, (2015).
435 33 Espinosa-Marzal, R. M., Han, M., Arcifa, A., Spencer, N. D. & Rossi, A. in *Encyclopedia of Interfacial
436   Chemistry*   (ed Klaus Wandelt) 172-194 (Elsevier, 2018).
437 34 Werzer, O., Cranston, E. D., Warr, G. G., Atkin, R. & Rutland, M. W. Ionic liquid nanotribology: mica–
438   silica interactions in ethylammonium nitrate. *Physical Chemistry Chemical Physics* **14**, 5147-5152,
439   (2012).
440 35 Voïtchovsky, K. Anharmonicity, solvation forces, and resolution in atomic force microscopy at the solid-
441   liquid interface. *Physical Review E* **88**, 022407, (2013).
442 36 Lin, X., Salari, M., Arava, L. M. R., Ajayan, P. M. & Grinstaff, M. W. High temperature electrical energy
443   storage: advances, challenges, and frontiers. *Chemical Society Reviews* **45**, 5848-5887, (2016).
444 37 Simon, P. & Gogotsi, Y. Capacitive Energy Storage in Nanostructured Carbon–Electrolyte Systems.
445   *Accounts of Chemical Research* **46**, 1094-1103, (2013).
446 38 Pech, D., Brunet, M., Durou, H., Huang, P., Mochalin, V., Gogotsi, Y., Taberna, P.-L. & Simon, P.
447   Ultrahigh-power micrometre-sized supercapacitors based on onion-like carbon. *Nature Nanotechnology* **5**,
448   651, (2010).
449 39 Xie, K., Qin, X., Wang, X., Wang, Y., Tao, H., Wu, Q., Yang, L. & Hu, Z. Carbon Nanocages as
450   Supercapacitor Electrode Materials. *Advanced Materials* **24**, 347-352, (2012).
451 40 Mao, X., Yang, X., Wu, J., Tian, W., Rutledge, G. C. & Hatton, T. A. Microwave-Assisted Oxidation of
452   Electrospun Turbostratic Carbon Nanofibers for Tailoring Energy Storage Capabilities. *Chemistry of
453   Materials* **27**, 4574-4585, (2015).
454 41 Mao, X. W., Simeon, F., Rutledge, G. C. & Hatton, T. A. Electrospun Carbon Nanofiber Webs with
455   Controlled Density of States for Sensor Applications. *Advanced Materials* **25**, 1309-1314, (2013).

17

456 42   Li, J. C., Ma, C., Chi, M. F., Liang, C. D. & Dudney, N. J. Solid Electrolyte: the Key for High-Voltage
457   Lithium Batteries. *Advanced Energy Materials* **5**, (2015).
458 43   Alshammary, B., Walsh, F. C., Herrasti, P. & Ponce de Leon, C. Electrodeposited conductive polymers
459   for controlled drug release: polypyrrole. *Journal of Solid State Electrochemistry*, 1-21, (2015).
460 44   Stern, M. C., Simeon, F., Herzog, H. & Hatton, T. A. Post-combustion carbon dioxide capture using
461   electrochemically mediated amine regeneration. *Energy & Environmental Science* **6**, 2505-2517, (2013).
462 45   Wang, L. D., Drahushuk, L. W., Cantley, L., Koenig, S. P., Liu, X. H., Pellegrino, J., Strano, M. S. &
463   Bunch, J. S. Molecular valves for controlling gas phase transport made from discrete angstrom-sized
464   pores in graphene. *Nature Nanotechnology* **10**, 785-+, (2015).
465 46   Hou, X., Hu, Y. H., Grinthal, A., Khan, M. & Aizenberg, J. Liquid-based gating mechanism with tunable
466   multiphase selectivity and antifouling behaviour. *Nature* **519**, 70-73, (2015).

467

Acknowledgments

474

Author contributions

X.M. and P.B. conceived the initial idea. X.M. designed and led the research, carried out electrochemical experiments, and analyzed experimental and simulation data, under the supervision of T.A.H. P.B. synthesized SAILs and contributed to electrochemical experiments, under the supervision of T.A.H. C.C. carried out MD simulations under the supervision of A.A.H.P. and M.F.C.G. G.H. performed SANS experiments under the supervision of J.E. and I.G. H.L. performed AFM force measurements under the supervision of R.A. Y.R. contributed to synthesis of SAILs and x-ray reflectivity measurements. D.C. performed x-ray reflectivity measurements. X.M. wrote the manuscript. All authors revised the manuscript.

484

Competing interests

X.M., P.B., M.F.C.G., and T.A.H. have filed a patent application based on this work. Title: HIGH-TEMPERATURE SUPERCAPACITORS CONTAINING SURFACE ACTIVE IONIC LIQUIDS. Filed

488   with the U.S. Patent and Trademark Office (U.S. Patent Application No.: 16/323,468) on February 5,

489   2019, and published on June 20, 2019 with Publication No. US-2019-0189364-A1.

Methods

Synthesis of SAILs. 1-Butyl-3-methyl-imidazolium chloride ([C_4C_1Im][Cl], ≥99%) was purchased from Sigma-Aldrich and used as received. Aerosol-OT (AOT, sodium 1,4-bis(2-ethylhexoxy)-1,4-dioxobutane-2-sulfonate) was purchased from Sigma-Aldrich and purified by Soxhlet extraction using dry acetone and subjected to repeated centrifugation. Ethyl acetate (≥99.5%) was purchased from Sigma-Aldrich and used without further purification. The ionic liquid 1-butyl-3-methylimidazolium 1,4-bis(2-ethylhexoxy)-1,4-dioxobutane-2-sulfonate, [C_4C_1Im][AOT] was synthesized via an ion-exchange technique[19] using a strong ion exchange resin (Amberlite IR 120 H$^+$ form) as follows: surfactant (sodium salt, 50 mmol) dissolved in 100ml EtOH/H_2O (1:1 v/v) and passed through a column (20 cm x 2 cm^2) of the ion exchange resin. For synthesis of [C_4C_1Im][C_8SO_4], [C_4C_1Im][$C_{10}SO_4$] and [C_4C_1Im][$C_{12}SO_4$], Sodium octyl sulfate (>99.0%, [Na][C_8SO_4]), sodium decyl sulfate (>99.0%, [Na][$C_{10}SO_4$]), and sodium dodecyl sulfate (>99.0%, [Na][$C_{12}SO_4$]) were purchased form Sigma Aldrich and used without further purification. These surfactants were also converted into ionic liquids via an ion-exchange technique as for the [C_4C_1Im][AOT]. Details on the synthesis and characterization of SAILs are presented in Supplementary Note 1.

Small-angle neutron scattering. Scattering was measured on the D22 diffractometer at ILL, Grenoble, France. A neutron wavelength of λ = 10 Å was employed at two different detector distances, giving $0.0024 < Q < 0.37$ Å^{-1}. Data normalization using accepted procedures gave the absolute cross section $I(Q)$ (cm^{-1}) as a function of momentum transfer Q (Å^{-1}). Samples were placed in Hellma fused silica cuvettes: path length 2 mm. Additional data analysis procedures are discussed in Supplementary Note 2.

Electrochemical experiments. All electrochemical measurements of the supercapacitor devices were carried out with a VersaSTAT4 potentiostat (Princeton Applied Research) in a two-electrode electrochemical cell thermostatted at the temperature of interest (± 1 °C). For the construction of the MWCNT supercapacitor devices[40], two pieces of MWCNT-deposited Toray carbon paper (active area = 2 cm^2, mass loading = 2.67 mg/cm^2) were assembled with a VWR filter paper sandwiched between them as the separator. The entire assembly was then sandwiched between two microscope glass slides, and dipped in the ionic liquid of interest. The two Toray carbon papers were attached to conductive copper tapes, which were connected to the potentiostat via alligator clips. The SWCNT and AC supercapacitor devices were assembled similarly as in the case of MWCNTs. Electrochemical impedance measurements were performed in a three-electrode system that consists of i) a flat-surface working

520 electrode (either glassy carbon electrode with a diameter of 3.0 mm, or Au electrode with 99.95% purity

521 and a diameter of 3.0 mm), ii) a Ag/Ag$^+$ reference electrode made of a silver wire, 10 mM AgBF$_4$, the

522 respective ionic liquid inside a glass tube with a porous CoralPor™ tip, and iii) a platinum gauze

523 auxiliary electrode (90/10 platinum/iridium alloy, 50.0 mm height, 38.0 mm diameter). The

524 heterogeneous electron transfer kinetics on the selected electrode were measured by sampled current

525 voltammetry (SCV)[47] using an electrolyte solution consisting of 1 mM Ru(NH$_3$)$_6^{3+/2+}$ and 1.0 M KCl.

526 Details of electrochemical characterizations are presented in Supplementary Note 3.

527 **Molecular dynamics simulation**. The [C$_4$C$_1$im]$^+$ cation[48,49] and the [BF$_4$]$^-$ anion were represented by

528 the CL&P all-atom nonpolarizable force field[50]. For the [AOT]$^-$, [DDS]$^-$, and [TC]$^-$ anions, the force

529 field parameters were assembled from existing values of similar molecules containing sulphonate, ether,

530 and alkyl chain groups from OPLS-AA[51,52] and are listed in Supplementary Table 1-4. The atom types

531 are illustrated in Supplementary Fig. 1. The graphite layers were modeled using the parameterization of

532 Girifalco *et al.*[53] Molecular dynamic simulations were performed using the LAMMPS[54] software

533 package with the Verlet integrator[55]. Short-range forces (Lennard-Jones) were cut-off at 12 Å of

534 interatomic separation and long-range electrostatic forces calculated with the particle-particle particle-

535 mesh (PPPM)[56] method. The SHAKE algorithm[57] was employed to keep length of the bonds terminating

536 in hydrogen atoms constant, enabling to use the time step of 1 fs for the simulations with constant

537 electrode charge density. Alternative simulations, during which the electrodes are kept at a constant

538 electrostatic potential difference, were run using the constant potential method (CPM) developed by

539 Siepman *et al.*[58] and Reed *et al.*[59] and implemented in LAMMPS by Wang *et al.*[60] Details on the MD

540 simulations are presented in Supplementary Note 4.1.

541 **Atomic force microscopy.** Force-distance profiles were performed using a Veeco NanoScope IV AFM.

542 Three sharp silicon cantilevers (spring constant 0.3±0.1 N/m) from the same batch (model NSC36,

543 Mikromasch, Tallinn, Estonia) were used over the course of the investigation. The cantilevers were

544 cleaned prior to use by careful rinsing in Milli-Q water and ethanol, drying under nitrogen and

545 irradiation with ultraviolet light for 20 min. An AFM electrochemistry fluid cell (MMTMEC, Bruker)

546 was used to hold ionic liquids on an HOPG surface during the measurements. HOPG was used as both

547 the working electrode and the solid substrate for AFM measurements. Pt wires of 0.25 mm were used as

548 both the counter and "quasi" reference electrodes. More details on the AFM measurements can be found
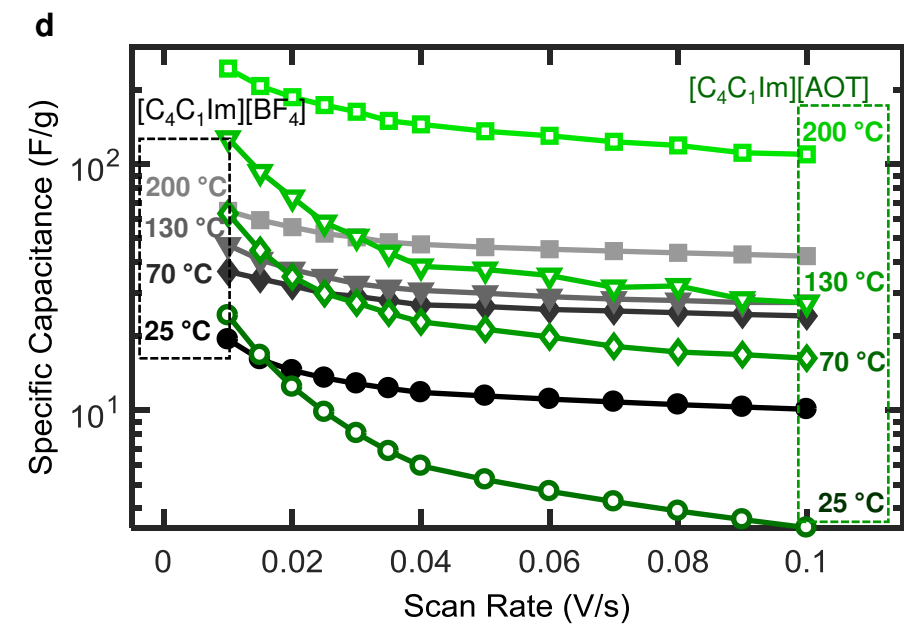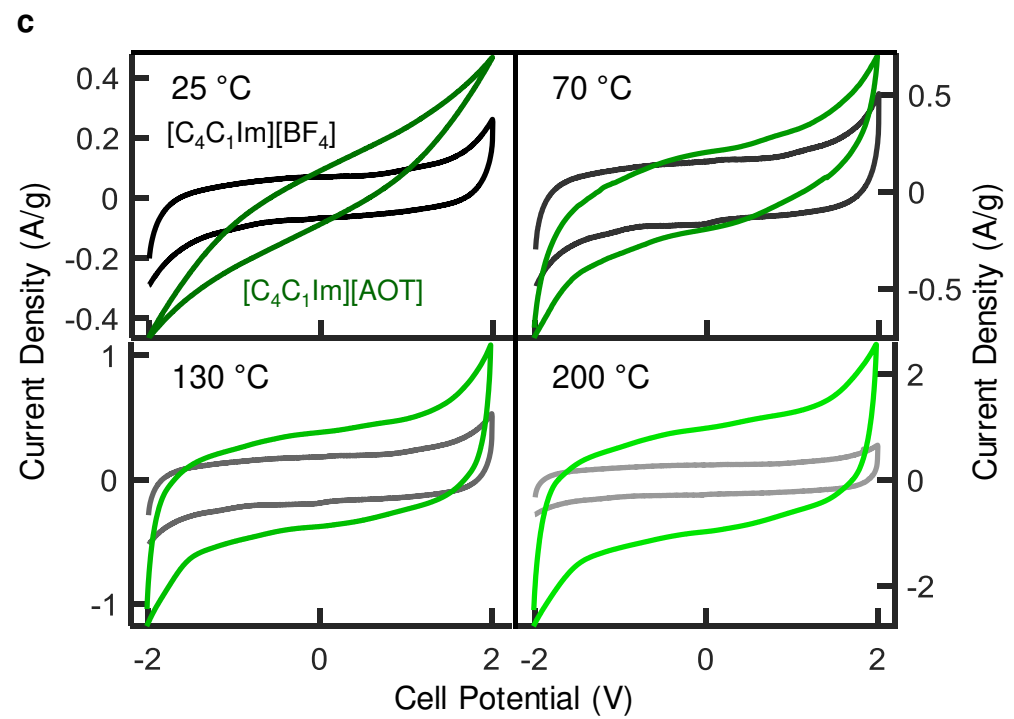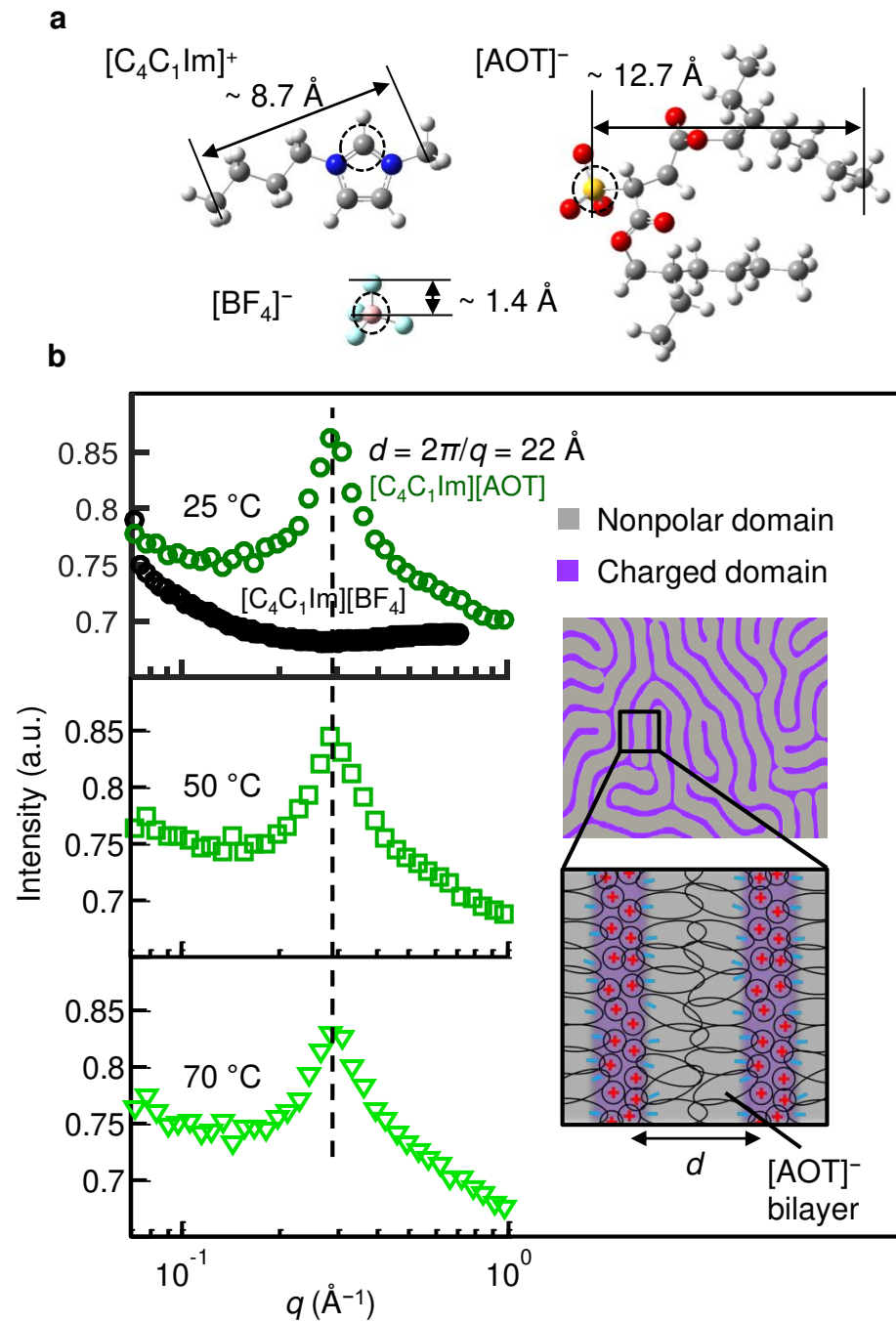
549 in Supplementary Note 5.

550

Data availability

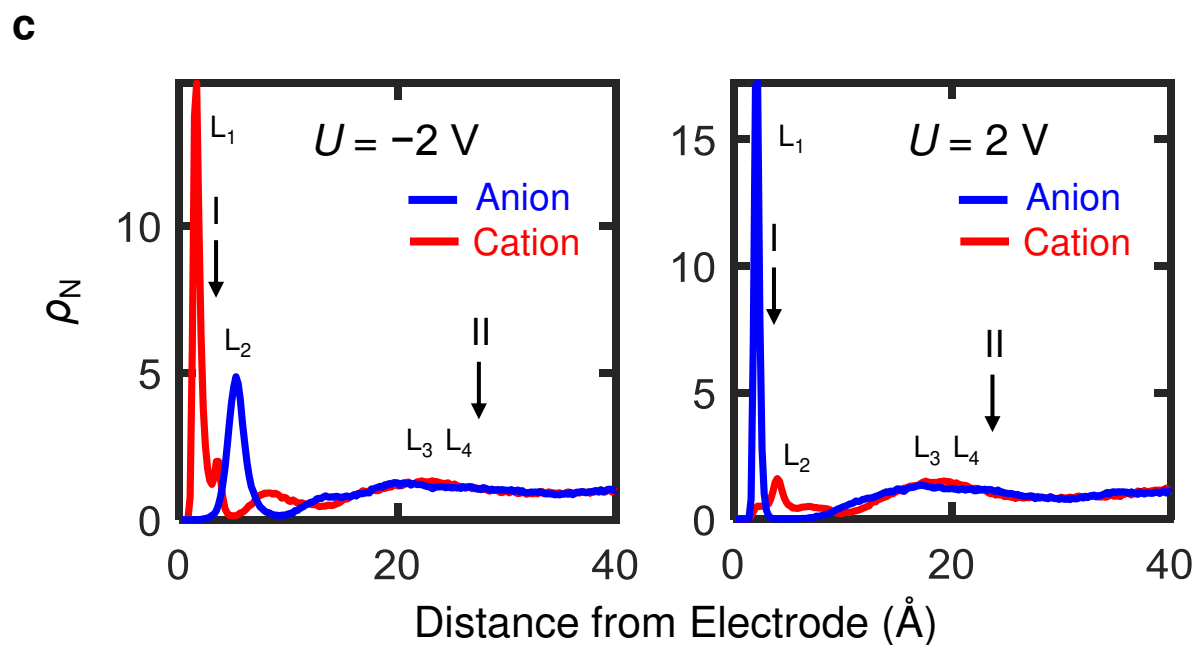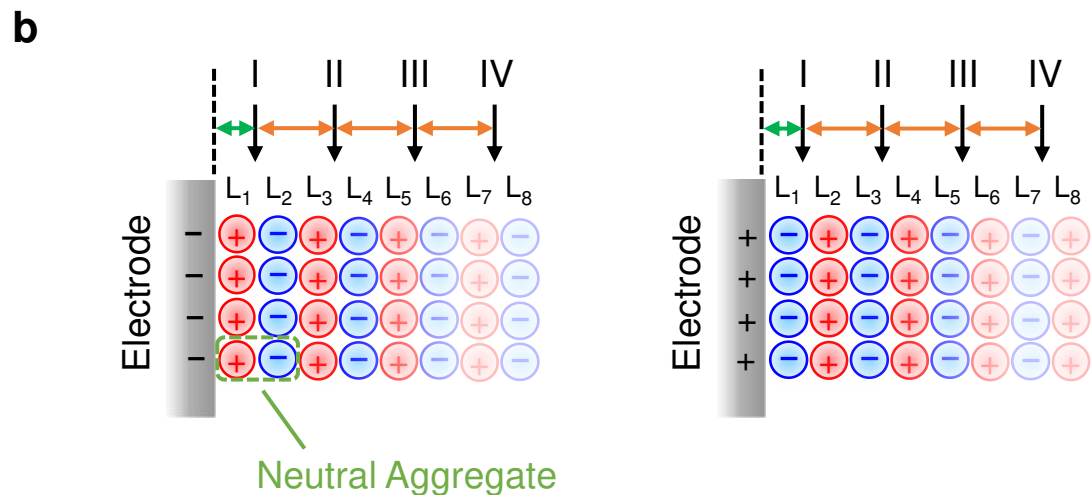The data that support the findings of this study are available from the corresponding authors upon reasonable request.

554

References

19   Brown, P., Butts, C. P., Eastoe, J., Fermin, D., Grillo, I., Lee, H.-C., Parker, D., Plana, D. & Richardson, R. M. Anionic Surfactant Ionic Liquids with 1-Butyl-3-methyl-imidazolium Cations: Characterization and Application. *Langmuir* **28**, 2502-2509, (2012).

40   Mao, X., Yang, X., Wu, J., Tian, W., Rutledge, G. C. & Hatton, T. A. Microwave-Assisted Oxidation of Electrospun Turbostratic Carbon Nanofibers for Tailoring Energy Storage Capabilities. *Chemistry of Materials* **27**, 4574-4585, (2015).

47   Mao, X., Guo, F., Yan, E. H., Rutledge, G. C. & Hatton, T. A. Remarkably High Heterogeneous Electron Transfer Activity of Carbon-Nanotube-Supported Reduced Graphene Oxide. *Chemistry of Materials* **28**, 7422-7432, (2016).

48   Canongia Lopes, J. N., Deschamps, J. & Padua, A. A. H. Modeling Ionic Liquids Using A Systematic All-Atom Force Field. *J Phys. Chem. B* **108**, 2038-2047, (2004).

49   Kaminski, G. A. & Jorgensen, W. L. Host-Guest Chemistry Of Rotaxanes And Catenanes: Application Of A Polarizable All-Atom Force Field To Cyclobis(Paraquat-P-Phenylene) Complexes With Disubstituted Benzenes And Biphenyls. *J. Chem. Soc., Perkin Trans. 2* **11**, 2365-2375, (1999).

50   Canongia Lopes, J. N. & Padua, A. A. H. CL&P: A Generic And Systematic Force Field For Ionic Liquids Modeling. *Theor. Chem. Acc.* **131**, 1129, (2012).

51   Canongia Lopes, J. N., Pádua, A. A. H. & Shimizu, K. Molecular Force Field for Ionic Liquids IV: Trialkylimidazolium and Alkoxycarbonyl-Imidazolium Cations; Alkylsulfonate and Alkylsulfate Anions. *The Journal of Physical Chemistry B* **112**, 5039-5046, (2008).

52   Price, M. L. P., Ostrovsky, D. & Jorgensen, W. L. Gas-phase and liquid-state properties of esters, nitriles, and nitro compounds with the OPLS-AA force field. *Journal of Computational Chemistry* **22**, 1340-1352, (2001).

53   Girifalco, L. A., Hodak, M. & Lee, R. S. Carbon nanotubes, buckyballs, ropes, and a universal graphitic potential. *Physical Review B* **62**, 13104-13110, (2000).

54   Plimpton, S. Fast Parallel Algorithms For Short-Range Molecular-Dynamics. *J. Comp. Phys.* **117**, 1-19, (1995).

55   Tuckerman, M. E., Alejandre, J., Lopez-Rendon, R., Jochim, A. L. & Martyna, G. J. A Liouville-Operator Derived. Measure-Preserving Integrator For Molecular Dynamics Simulations In The Isothermal-Isobaric Ensemble. *J. Phys. A: Math. Gen* **39**, 5629-5651, (2006).

56   Hockney, R. W. & Eastwood, J. W. *Computer Simulation Using Particles*. (Taylor&Francis, 1988).

57   Ryckaert, J. P., Ciccotti, G. & Berendsen, H. J. C. Numerical-Integration Of Cartesian Equations Of Motion Of A System With Constraints - Molecular-Dynamics Of n-Alkanes. *J. Comp. Phys.* **23**, 327-341, (1977).

58   Siepmann, J. I. & Sprik, M. Influence of surface topology and electrostatic potential on water/electrode systems. *The Journal of chemical physics* **102**, 511-524, (1995).

59   Reed, S. K., Lanning, O. J. & Madden, P. A. Electrochemical interface between an ionic liquid and a model metallic electrode. *The Journal of Chemical Physics* **126**, 084704, (2007).

593   60   Wang, Z., Yang, Y., Olmsted, D. L., Asta, M. & Laird, B. B. Evaluation of the constant potential method
594   in simulating electric double-layer capacitors. *The Journal of Chemical Physics* **141**, 184102, (2014).

595

a [C₄C₁Im]⁺ ~ 8.7 Å   [AOT]⁻ ~ 12.7 Å

[BF₄]⁻ ~ 1.4 Å

b $d = 2\pi/q = 22$ Å

[C₄C₁Im][AOT]

25 °C

[C₄C₁Im][BF₄]

50 °C

70 °C

Nonpolar domain

Charged domain

[AOT]⁻ bilayer

d

Intensity (a.u.)

q (Å⁻¹)

c

25 °C   [C₄C₁Im][BF₄]   70 °C

[C₄C₁Im][AOT]

130 °C   200 °C

Current Density (A/g)

Cell Potential (V)

d

[C₄C₁Im][BF₄]   [C₄C₁Im][AOT]

200 °C

130 °C

70 °C

25 °C

200 °C

130 °C

70 °C

25 °C

Specific Capacitance (F/g)

Scan Rate (V/s)

b

Neutral Aggregate

c

ρ_N

$U = -2$ V — Anion, Cation

$U = 2$ V — Anion, Cation

Distance from Electrode (Å)

d

f

ρ_N (Anion)

ρ_Q (C/mm³)

$U = -2$ V

$[C_4C_1Im][BF_4]$

$[C_4C_1Im][AOT]$

$U = 2$ V

$[C_4C_1Im][BF_4]$

$[C_4C_1Im][AOT]$

Distance from Electrode (Å)

g

ξ (Å)

$[C_4C_1Im][BF_4]$

$[C_4C_1Im][AOT]$

U (V)

h

$[C_4C_1Im][AOT]$

a

25 °C

C_d (μF/cm^2)

[C$_4$C$_1$Im][BF$_4$]

U (V)

b

70 °C

[C$_4$C$_1$Im][BF$_4$]

C_d (μF/cm^2)

[C$_4$C$_1$Im][AOT]

U (V)

c

130 °C

[C$_4$C$_1$Im][AOT]

C_d (μF/cm^2)

[C$_4$C$_1$Im][BF$_4$]

U (V)

d

200 °C

[C$_4$C$_1$Im][AOT]

C_d (μF/cm^2)

[C$_4$C$_1$Im][BF$_4$]

U (V)

a [DDS]⁻   [TC]⁻

b
$\sigma = -10\ \mu\text{C/cm}^2$

$\sigma = 10\ \mu\text{C/cm}^2$

[C₄C₁Im][TC]

[C₄C₁Im][DDS]

[C₄C₁Im][BF₄]

ρ_Q (C/mm³)

Distance from Electrode (Å)

c

[C₄C₁Im][DDS]

[C₄C₁Im][BF₄]

ξ (Å)

d
Low Temperature   High Temperature

Z-Axis   Z-Axis

Confining Surface   Nonpolar Domain

e
[C₄C₁Im][BF₄]

Cation

Anion

[C₄C₁Im][DDS]

[C₄C₁Im][AOT]

[C₄C₁Im][TC]

ρ_N

a

$[C_4C_1Im][C_8SO_4]$

70 °C
50 °C
25 °C
26 Å

$[C_4C_1Im][C_{10}SO_4]$

28 Å

Intensity (a.u.)

$[C_4C_1Im][C_{12}SO_4]$

20 Å
28 Å

b

$[C_4C_1Im][C_8SO_4]$

150
100
50
0

130 °C
25 °C

$[C_4C_1Im][C_{10}SO_4]$

200
100
0

130 °C
25 °C

Specific Capacitance (F/g)

$[C_4C_1Im][C_{12}SO_4]$

150
100
50

130 °C

3
2
1

4
3
2
1

3
2.5
2

Enhancement Relative to $[C_4C_1Im][BF_4]$